FCAF3D: Fully Convolutional Anchor-Free 3D Object Detection

Danila Rukhovich, Anna Vorontsova, Anton Konushin Samsung AI Center, Moscow

d.rukhovich, a.vorontsova, a.konushin@samsung.com

Abstract

Recently, promising applications in robotics and augmented reality have attracted considerable attention to 3D object detection from point clouds. In this paper, we present FCAF3D - a first-in-class fully convolutional anchor-free indoor 3D object detection method. It is a simple vet effective method that uses a voxel representation of a point cloud and processes voxels with sparse convolutions. FCAF3D can handle large-scale scenes with minimal runtime through a single fully convolutional feed-forward pass. Existing 3D object detection methods make prior assumptions on the geometry of objects, and we argue that it limits their generalization ability. To get rid of any prior assumptions, we propose a novel parametrization of oriented bounding boxes that allows obtaining better results in a purely data-driven way. The proposed method achieves state-of-the-art 3D object detection results in terms of mAP@0.5 on ScanNet V2 (+4.5), SUN RGB-D (+3.5), and S3DIS (+20.5) datasets. The code and models are available at https://github.com/samsunglabs/fcaf3d.

1. Introduction

3D object detection from point clouds aims at simultaneous localization and recognition of 3D objects from a 3D point set. As a core technique for 3D scene understanding, it is widely applied in autonomous driving, robotics manipulation, and AR.

While 2D methods [26, 32] work with dense fixed-size arrays, 3D methods are challenged by irregular unstructured 3D data of arbitrary volume. Consequently, the data processing techniques that proved to be efficient in 2D object detection are not directly applicable for 3D object detection. Therefore, 3D object detection methods [10,19,22] propose inventive approaches to 3D data processing.

All convolutional methods for 3D object detection have scalability issues: large-scale scenes either require an impractical amount of computational resources or take too much time to process. Other methods opt for voxel data rep-

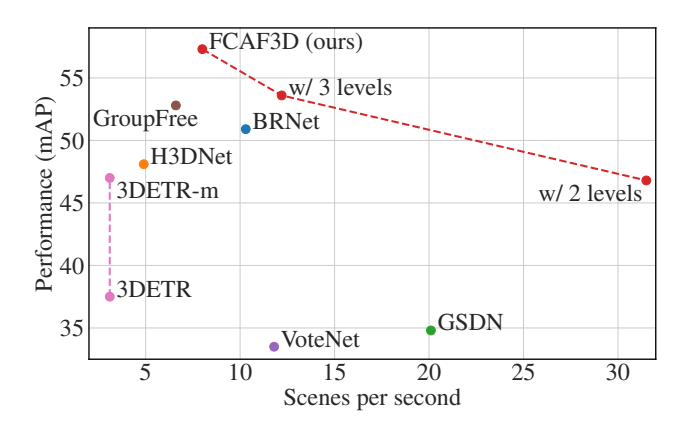


Figure 1. mAP@0.5 scores on ScanNet against scenes per second. FCAF3D modifications (marked red) have different number of backbone feature levels. For each existing method, there is a FCAF3D modification surpassing this method in both detection accuracy and inference speed.

resentation and employ sparse convolutions; however, these methods solve scalability problems at the cost of detection accuracy. In other words, there is no 3D object detection method that provides precise estimates and scales well at the same time.

Besides being scalable and accurate, an ideal 3D object detection method should also be able to handle diverse objects of arbitrary shapes and sizes without additional hacks and hand-tuned hyperparameters. We argue that any prior assumptions on 3D object bounding boxes (e.g. aspect ratios or absolute sizes of these bounding boxes) restrict the generalization ability and increase the number of hyperparameters and trainable parameters. Without such priors, these methods demonstrate an accuracy drop.

On the contrary, we do not want to rely on any prior assumptions. We propose an anchor-free method that does not impose priors on objects and addresses 3D object detection with a purely data-driven approach. Moreover, we introduce a novel oriented bounding box (OBB) parametrization inspired by a Mobius strip that reduces the number of hyperparameters. To prove the effectiveness of our parametrization, we conduct experiments on SUN RGB-D with several

3D object detection methods and report improved results for all these methods.

In this paper, we introduce FCAF3D - a simple, effective and scalable method for detecting 3D objects from point clouds. We evaluate the proposed method on Scan-Net [7], SUN RGB-D [25], and S3DIS [1] benchmark, demonstrating the solid superiority over the previous state-of-the-art on all benchmarks. On SUN RGB-D and Scan-Net datasets, our method surpasses other methods by at least 3.5% mAP@0.5. On S3DIS, FCAF3D outperforms the current state-of-the-art by a huge margin.

Overall, our contribution is three-fold:

- 1. To our knowledge, we propose a first-in-class fully convolutional anchor-free 3D object detection method (FCAF3D) for indoor scenes.
- We present a novel OBB parametrization and prove it to boost accuracy of several existing 3D object detection methods on SUN RGB-D.
- Our method significantly outperforms the previous state-of-the-art on challenging large-scale indoor ScanNet, SUN RGB-D, and S3DIS datasets in terms of mAP while being faster on inference.

2. Related Work

The most recent 3D object detection methods are designed to be either indoor or outdoor. Indoor and outdoor methods have been developing almost independently, applying domain-specific solutions to address data issues. Many modern outdoor methods [13, 30, 35] project 3D points onto a bird-eye-view plane, thus reducing the task of 3D object detection to 2D object detection. Naturally, these methods take advantage of the fast-evolving algorithms for 2D object detection. Given a bird-eye-view projection, [14] processes it in a fully convolutional manner, while [31] exploits 2D anchor-free approach. Unfortunately, the approaches that proved to be effective for both 2D object detection and 3D outdoor object detection cannot be trivially adapted to indoor, as it would require an impracticable amount of memory and computing resources. To address performance issues, different 3D data processing strategies have been proposed. Currently, three approaches dominate the field of 3D object detection - voting-based, transformerbased, and 3D convolutional. Below we discuss each of these approaches in detail; in addition, we provide a brief overview of anchor-free methods.

Voting-based methods. VoteNet [22] was the first method that introduced points voting for 3D object detection. VoteNet processes 3D points with PointNet [23], assigns a group of points to each object candidate according to their voted center and then computes object features from each point group. Among the numerous successors of

VoteNet, the major progress was associated with advanced grouping and voting strategies on top of the PointNet features. BRNet [4] refines voting results with the second voting focusing the representative points from the vote centers, which improves capturing the fine local structural features. MLCVNet [29] introduces three context modules into the voting and classifying stages of VoteNet to encode contextual information at different levels. H3DNet [33] improves the point group generation procedure by predicting a hybrid set of geometric primitives. VENet [28] incorporates an attention mechanism and introduces a vote weighting module trained via a novel vote attraction loss.

All the voting-based methods inherited from VoteNet are limited by design. First, their performance depends on the amount of input data; thus, they tend to slow down if given larger scenes and demonstrate poor scalability. Moreover, many voting-based methods implement voting and grouping strategies as complex custom layers making it difficult to reproduce or debug these methods or port them to mobile devices.

Transformer-based methods. The recently emerged transformer-based methods use end-to-end learning and forward pass on inference instead of heuristics and optimization, which makes them less domain-specific. GroupFree [17] replaces VoteNet head with a transformer module, updating object query locations iteratively and ensembling intermediate detection results. 3DETR [19] was the first method of 3D object detection implemented as an end-to-end trainable transformer. However, similar to early voting-based methods, more advanced transformer-based methods still experience scalability issues. Differently, our method is fully-convolutional thus being faster and significantly easier to implement compared to both voting-based and transformer-based methods.

3D convolutional methods. Difficulties with handling cubically growing sparse 3D data can be overcome by using voxel representation. Voxel-based 3D object detection methods [12, 18] convert points into voxels and process them with 3D convolutional networks. However, dense volumetric features still consume much memory, and 3D convolutions are computationally expensive. Overall, processing large scenes requires a lot of resources and cannot be done within a single pass.

GSDN [10] addresses performance issues by employing sparse 3D convolutions. It has encoder-decoder architecture, with both encoder and decoder parts built from sparse 3D convolutional blocks. Compared to the standard convolutional voting-based and transformer-based approaches, GSDN is significantly more memory-efficient and scales to large scenes without sacrificing point density. The major weakness of this approach is its accuracy: in terms of quality, this method is comparable to VoteNet, being significantly inferior to the current state-of-the-art [17].

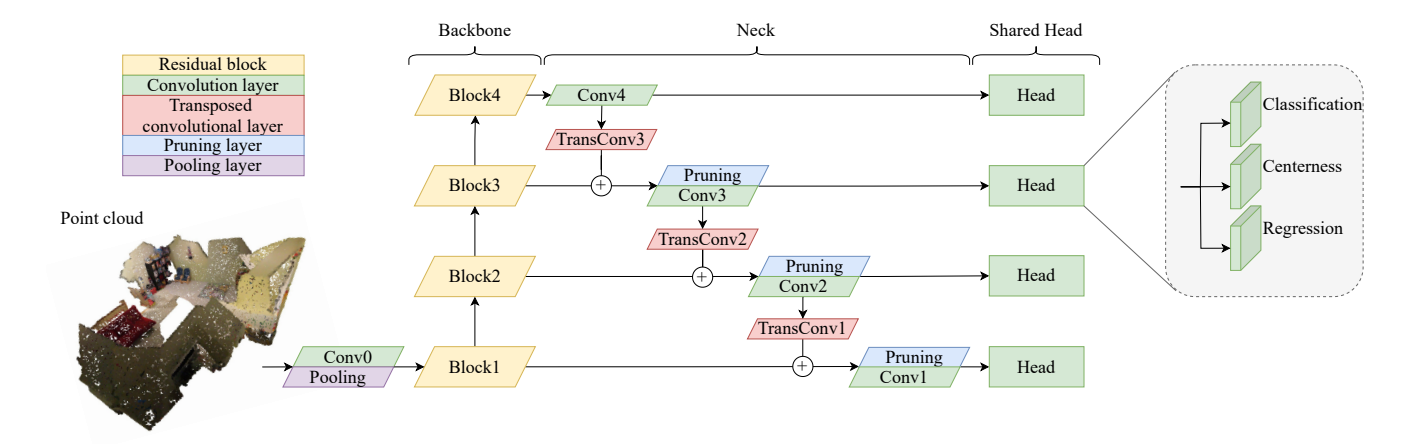


Figure 2. The general scheme of the proposed FCAF3D. All convolutions and transposed convolutions are three-dimensional and sparse. This design allows processing the input point cloud in a single forward pass.

GSDN uses 15 aspect ratios for 3D object bounding boxes as anchors. If GSDN is trained in anchor-free setting with a single aspect ratio, the accuracy decreases by 12%. At the same time, our method is anchor-free while taking all advantages of sparse 3D convolutions.

RGB-based anchor-free object detection. In 2D object detection, anchor-free methods have recently become solid competitors for the standard anchor-based methods. FCOS [26] solves the 2D object detection problem in a perpixel prediction manner and shows a robust improvement over its anchor-based counterpart RetinaNet [15]. FCOS3D [27] trivially adapts the ideas of FCOS by introducing extra targets for monocular 3D object detection. ImVoxelNet [24] solves the same problem with an FCOS-like head built from standard (non-sparse) 3D convolutional blocks. We adapt the ideas from aforementioned anchor-free methods to address the sparse irregular data.

3. Proposed Method

Following the standard 3D detection problem statement, FCAF3D accepts $N_{\rm pts}$ RGB-colored points and outputs a set of 3D object bounding boxes. The architecture of FCAF3D consists of three parts: a backbone, a neck, and a head (depicted in Fig. 2).

While designing FCAF3D, we aim for scalability, so we opt for a GSDN-like sparse convolutional network. For better generalization, we reduce the number of hyperparameters in this network that need to be manually tuned; specifically, we simplify sparsity pruning in the neck. Furthermore, we introduce an anchor-free head with a simple multi-level location assignment. Finally, we discuss the limitations of existing 3D bounding box parametrizations and propose a novel parametrization that improves both accuracy and generalization ability.

3.1. Sparse Neural Network

Backbone. The backbone in FCAF3D is a sparse modification of ResNet [11] where all 2D convolutions are replaced with sparse 3D convolutions. The family of sparse high-dimensional versions of ResNet was first introduced in [5]; for brevity, we refer to them as to HDResNet.

Neck. The neck is a simplified decoder from GSDN. Features on each level are processed with one sparse transposed 3D convolution and one sparse 3D convolution. Each transposed sparse 3D convolution with a kernel size of 2 can increase the number of non-zero values by 2^3 times. To prevent the rapid growth of required memory, GSDN introduces the *pruning* layer that filters all elements of input with a probability mask.

In GSDN, feature level-wise probabilities are calculated with an additional convolutional scoring layer. This layer is trained with a special loss that encourages consistency between the predicted sparsity and anchors. Specifically, voxel sparsity is set to be positive if any of the subsequent anchors associated to the current voxel is positive. However, using this loss may be suboptimal, as distant voxels of an object might get assigned with a low probability.

For simplicity, we remove the scoring layer with the corresponding loss and use probabilities from the classification layer in the head instead. We do not tune the probability threshold but keep at most $N_{\rm vox}$ voxels to control the sparsity level, where $N_{\rm vox}$ equals the number of input points $N_{\rm pts}$. We claim this to be a simple yet elegant way to prevent sparsity growth since reusing the same hyperparameter makes the process more transparent and consistent.

Head. The anchor-free head of FCAF3D consists of three parallel sparse convolutional layers with weights shared across feature levels. For each location $(\hat{x}, \hat{y}, \hat{z})$, these sparse convolutional layers output classification probabilities \hat{p} , bounding box regression parameters δ , and cen-

terness \hat{c} , respectively. This design is similar to the simple and light-weight head of FCOS [26] but adapted to 3D data.

Multi-level location assignment. During training, FCAF3D outputs locations $\{(\hat{x}, \hat{y}, \hat{z})\}$ for different feature levels, which should be assigned to ground truth boxes $\{b\}$ so the loss can be calculated. FCOS [26] and ImVoxel-Net [24] stick to the following scheme: for each location, only ground truth bounding boxes that cover this location are selected. Then, the bounding boxes with at least one face further from this location than a threshold are filtered out. Finally, the bounding box with the least volume is assigned to this location. Such an assignment strategy is suboptimal, and its alterations are widely explored in 2D object detection [9,32]. ImVoxelNet [24] uses a modification that requires hand-tuning the face distance threshold for each feature level.

We propose a simplified solution designed for sparse data that does not require tuning dataset-specific hyperparameters. For each bounding box, we select the last feature level for which this bounding box covers at least $N_{\rm loc}$ locations. If the bounding box covers less than $N_{\rm loc}$ locations at each feature level, we opt for the first feature level. We also filter locations via *center sampling* described in [26]. In center sampling, only the points close to the center of the bounding box are considered positive matches. More details are presented in Sec. 5.3.

After the location assignment, some final locations $\{(\hat{x},\hat{y},\hat{z})\}$ are matched with ground truth bounding boxes $b_{\hat{x},\hat{y},\hat{z}}$. Consequently, these locations become associated with ground truth labels $p_{\hat{x},\hat{y},\hat{z}}$ and 3D centerness values $c_{\hat{x},\hat{y},\hat{z}}$. During inference, the scores \hat{p} are multiplied by 3D centerness \hat{c} just before applying NMS as proposed in [24].

Loss function. The overall loss function is formulated as follows:

$$L = \frac{1}{N_{\text{pos}}} \sum_{\hat{x}, \hat{y}, \hat{z}} (L_{\text{cls}}(\hat{\boldsymbol{p}}, p) + \mathbb{1}_{\{p_{\hat{x}, \hat{y}, \hat{z}} \neq 0\}} L_{\text{reg}}(\hat{\boldsymbol{b}}, \boldsymbol{b}) + \mathbb{1}_{\{p_{\hat{x}, \hat{y}, \hat{z}} \neq 0\}} L_{\text{cntr}}(\hat{c}, c)).$$
(1)

Here, the number of matched locations $N_{\rm pos}$ is $\sum_{\hat{x},\hat{y},\hat{z}}\mathbb{1}_{\{p_{\hat{x},\hat{y}},\hat{z}\neq 0\}}$. Classification loss $L_{\rm cls}$ is calculated as a focal loss, regression loss $L_{\rm reg}$ is IoU, and centerness loss $L_{\rm cntr}$ is binary cross-entropy. For each loss, predicted values are denoted with a hat.

3.2. Bounding Box Parametrization

The 3D object bounding boxes can be axis-aligned (AABB) or oriented (OBB). An AABB can be described as ${\bf b}^{\rm AABB}=(x,y,z,w,l,h),$ while the definition of an OBB includes a heading angle $\theta\colon {\bf b}^{\rm OBB}=(x,y,z,w,l,h,\theta).$ In both formulas, x,y,z denote the coordinates of the center of a bounding box, while w,l,h are its width, length, and height, respectively.







Figure 3. Examples of objects with an ambiguous heading angle.

AABB parametrization. For AABBs, we follow the parametrization proposed in [24]. Specifically, for a ground truth AABB (x, y, z, w, l, h) and a location $(\hat{x}, \hat{y}, \hat{z})$, δ can be formulated as a 6-tuple:

$$\delta_{1} = x + \frac{w}{2} - \hat{x}, \ \delta_{2} = \hat{x} - x + \frac{w}{2}, \ \delta_{3} = y + \frac{l}{2} - \hat{y},$$

$$\delta_{4} = \hat{y} - y + \frac{l}{2}, \ \delta_{5} = z + \frac{h}{2} - \hat{z}, \ \delta_{6} = \hat{z} - z + \frac{h}{2}.$$
(2)

The predicted AABB \hat{b} can be trivially obtained from δ .

Heading angle estimation. All existing state-of-the-art 3D object detection methods from point clouds address the heading angle estimation task as classification followed by regression. The heading angle is classified into bins; then, the precise value of the heading angle is regressed within a bin. For indoor scenes, there are typically 12 bins that uniformly divide the range from 0 to 2π into 12 sectors [19, 21,22,33]. For outdoor scenes, the number of bins is usually set to two [13,30] as the objects on the road can be oriented either parallel or perpendicular to the road.

When a heading angle bin is chosen, the actual value of the heading angle should be estimated through regression. VoteNet and other voting-based methods estimate the value of missing θ directly. Outdoor methods explore more elaborate approaches, e.g. predicting the values of trigonometric functions. For instance, SMOKE [16] estimates the values of $\sin\theta$ and $\cos\theta$, which allows recovering the heading angle.

Fig. 3 depicts indoor objects where the heading angle cannot be defined unambiguously. Ground truth angle annotations are random for these objects, making heading angle bin classification meaningless. To avoid penalizing the correct predictions that do not coincide with annotations, we use rotated IoU as a loss function, since its value is not affected by the choice of a heading angle among possible options. Thus, we propose OBB parametrization that allows considering the rotation ambiguity.

Proposed Mobius OBB parametrization. Assuming that an OBB has the parameters (x,y,z,w,l,h,θ) , let us denote $q=\frac{w}{l}$. If $x,\ y,\ z,\ w+l,\ h$ are fixed, it turns out that the OBBs with

$$(q,\theta), \left(\frac{1}{q}, \theta + \frac{\pi}{2}\right), \left(q,\theta + \pi\right), \left(\frac{1}{q}, \theta + \frac{3\pi}{2}\right)$$
 (3)

define the same bounding box. We notice that the set of (q,θ) , where $\theta \in (0,2\pi], \ q \in (0,+\inf)$ is topologically equivalent to a Mobius strip [20] up to this equivalence relation. Hence, we can reformulate the task of estimating (q,θ) as a task of predicting a point on a Mobius strip. A natural way to embed a Mobius strip being a two-dimensional manifold to Euclidean space is the following:

$$(q, \theta) \mapsto (\ln(q)\sin(2\theta), \ln(q)\cos(2\theta), \sin(4\theta), \cos(4\theta)).$$
 (4)

It is easy to verify that 4 points from Eq. 3 are mapped into a single point in Euclidean space (see Sec. A). However, the experiments reveal that predicting only $\ln(q)\sin(2\theta)$ and $\ln(q)\cos(2\theta)$ improves results compared to predicting all four values. Thereby, we opt for a *pseudo* embedding of a Mobius strip to \mathbb{R}^2 . We call it *pseudo* since the entire center circle of a Mobius strip defined by $\ln(q)=0$ maps to (0,0). Accordingly, we cannot distinguish points with $\ln q=0$. However, $\ln(q)=0$ implies strict equality of w and v0, which is rare in real-world scenarios. Moreover, the choice of an angle has a minor effect on the IoU if v1, thereby, we ignore this rare case for the sake of detection accuracy and simplicity of the method. Overall, we obtain a novel OBB parametrization:

$$\delta_7 = \ln \frac{w}{l} \sin(2\theta), \ \delta_8 = \ln \frac{w}{l} \cos(2\theta).$$
 (5)

In standard 3D bounding box parametrization 2, \hat{b} is trivially derived from δ . In the proposed parametrization, w, l, θ are non-trivial and can be obtained via the following:

$$w = \frac{sq}{1+q}, \ l = \frac{s}{1+q}, \ \theta = \frac{1}{2}\arctan\frac{\delta_7}{\delta_8},$$
 (6)

where ratio $q = e^{\sqrt{\delta_7^2 + \delta_8^2}}$ and size $s = \delta_1 + \delta_2 + \delta_3 + \delta_4$.

4. Experiments

4.1. Datasets

We evaluate our method on three 3D object detection benchmarks: ScanNet V2 [7], SUN RGB-D [25], and S3DIS [1]. For all datasets, we use mean average precision (mAP) under IoU thresholds of 0.25 and 0.5 as a metric.

ScanNet. The ScanNet dataset contains 1513 reconstructed 3D indoor scans with per-point instance and semantic labels of 18 object categories. Given this annotation, we calculate AABBs through a standard approach [22]. The training subset is comprised of 1201 scans, while the resting 312 scans are left for validation.

SUN RGB-D. SUN RGB-D is a monocular dataset for 3D scene understanding containing more than 10,000 indoor RGB-D images. The annotation consists of per-point semantic labels and OBBs of 37 object categories. As proposed in [22], we run experiments with objects of the 10

most common categories. The training and validation splits contain 5285 and 5050 point clouds, respectively.

S3DIS. Stanford Large-Scale 3D Indoor Spaces dataset contains 3D scans of 6 buildings with 272 rooms. Each scan is annotated with instance and semantic labels of seven structural elements (e.g. *floor* and *ceiling*) and five furniture categories. Following [10], we evaluate our method on furniture categories only. Similar to ScanNet, AABBs are derived from 3D semantics. We use the official split, where 68 rooms from *Area 5* are intended for validation, while the remaining 204 rooms comprise the training subset.

4.2. Implementation Details

Hyperparameters. For all datasets, we use the same hyperparameters except for the following. First, the size of output classification layer equals the number of object categories, which is 18, 10, and 5 for ScanNet, SUN RGB-D, and S3DIS. Second, SUN RGB-D contains OBBs, so we predict additional targets δ_7 and δ_8 for this dataset; note that the loss function is not affected. Last, ScanNet, SUN RGB-D, and S3DIS contain different numbers of scenes, so we repeat each scene 10, 3, and 13 times per epoch, respectively.

Similar to GSDN [10], we use the sparse 3D modification of ResNet34 named HDResNet34 as a backbone. The neck and the head use the outputs of the backbone at all feature levels. In initial point cloud voxelization, we set the voxel size to 0.01m and the number of points $N_{\rm pts}$ to 100,000. Respectively, $N_{\rm vox}$ equals to 100,000. Both ATSS [32] and FCOS [26] set $N_{\rm loc}$ to 3^2 for 2D object detection. Accordingly, we select a feature level so bounding box covers at least $N_{\rm loc}=3^3$ locations. By center sampling, we select 18 locations, while the NMS IoU threshold is 0.5.

Training. We implement our FCAF3D using the MMdetection3D [6] framework. The overall training procedure follows the default scheme from MMdetection [3]: training takes 12 epochs with the learning rate decreasing on the 8th and the 11th epochs. We employ the Adam optimizer with an initial learning rate of 0.001 and weight decay of 0.0001. All models are trained on two NVidia V100 with a batch size of 8. Evaluation and performance tests are run on a single NVidia GTX1080Ti.

Evaluation. We follow the evaluation protocol introduced in [17]. Both training and evaluation procedures are randomized, as the raw point clouds are randomly sampled to select $N_{\rm pts}$ for the input. Thus, we re-run all the experiments to obtain statistically significant results. We run training 5 times and test each trained model 5 times independently. We report both the best and average metrics across all 5×5 trials. Eventually, this evaluation protocol allows directly comparing FCAF3D to the 3D object detection methods that report either a single best or an average value.

Method	Presented at	Scar	Net	SUN R	GB-D	S3I	OIS
Method	r resemed at	mAP@0.25	mAP@0.5	mAP@0.25	mAP@0.5	mAP@0.25	mAP@0.5
VoteNet [22]	ICCV'19	58.6	33.5	57.7	-	-	-
3D-MPA [8]	CVPR'20	64.2	49.2	-	-	-	-
HGNet [2]	CVPR'20	61.3	34.4	61.6	-	-	-
MLCVNet [29]	CVPR'20	64.5	41.4	59.8	-	-	-
GSDN [10]	ECCV'20	62.8	34.8	-	-	47.8	25.1
H3DNet [33]	ECCV'20	67.2	48.1	60.1	39.0	-	-
BRNet [4]	CVPR'21	66.1	50.9	61.1	43.7	-	-
3DETR [19]	ICCV'21	65.0	47.0	59.1	32.7	-	-
VENet [28]	ICCV'21	67.7	-	62.5	39.2	-	-
GroupFree [17]	ICCV'21	69.1 (68.6)	52.8 (51.8)	63.0 (62.6)	45.2 (44.4)	-	-
FCAF3D	-	71.5 (70.7)	57.3 (56.0)	64.2 (63.8)	48.9 (48.2)	66.7 (64.9)	45.9 (43.8)

Table 1. Results of FCAF3D and existing indoor 3D object detection methods that accept point clouds. The best metric values are marked bold. FCAF3D outperforms previous state-of-the-art methods: GroupFree (on ScanNet and SUN RGB-D) and GSDN (on S3DIS). The reported metric value is the best one across 25 trials; the average value is given in brackets.

5. Results

5.1. Comparison with State-of-the-art Methods

We compare FCAF3D with previous state-of-the-arts on all three indoor benchmarks. The results are presented in Tab. 1. As one might observe, FCAF3D achieves the best results on all three benchmarks in terms of both mAP@0.25 and mAP@0.5. In terms of mAP@0.5, the performance gap is especially tangible: our method surpasses previous state-of-the-art by 4.5% on ScanNet and 3.7% on SUN RGB-D. For S3DIS, FCAF3D outperforms weak state-of-the-art by a huge margin. Overall, the proposed method is consistently better than existing methods, setting a new state-of-the-art for indoor 3D object detection. The examples of point clouds from ScanNet, SUN RGB-D and S3DIS with predicted bounding boxes are depicted in Fig. 4, 5, 6.

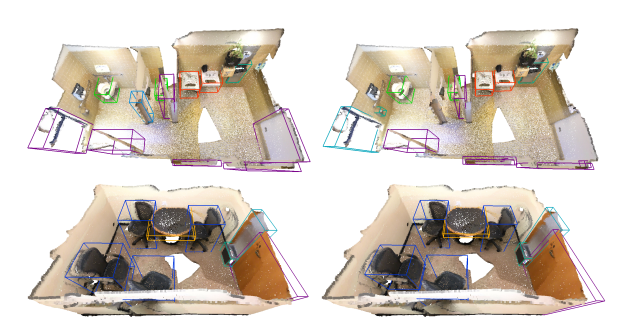


Figure 4. The point cloud from ScanNet with AABBs. The color of a bounding box denotes the object category. Left: estimated with FCAF3D, right: ground truth.

5.2. Object Geometry Priors

To study geometry priors, we train and evaluate existing methods with proposed modifications. For this study, we

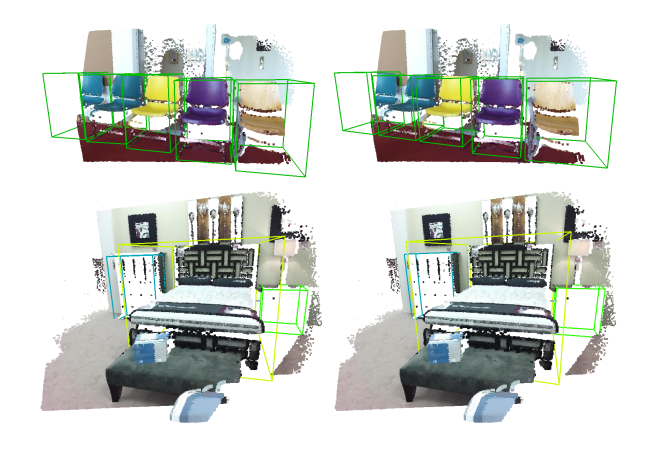


Figure 5. The point cloud from SUN RGB-D with OBBs. The color of a bounding box denotes the object category. Left: estimated with FCAF3D, right: ground truth.



Figure 6. The point cloud from S3DIS with AABBs. The color of a bounding box denotes the object category. Left: estimated with FCAF3D, right: ground truth.

have chosen 3D object detection methods that accept data of different modalities: point clouds, RGB images, or both, to see whether the effect is data-specific or universal. VoteNet and ImVoteNet have the same head and are trained with the same losses. Among them, there are 4 prior losses: size classification loss, size regression loss, direction classification loss, and direction regression loss. Both classification losses correspond to targets parametrized using priors (percategory mean object sizes and a set of angle bins). Similar to FCAF3D, we replace the aforementioned losses with a rotated IoU loss with Mobius parametrization 5. To give a complete picture, we also try a *sin-cos* parametrization used in the outdoor 3D object detection method SMOKE [16].

The rotated IoU loss allows decreasing the number of trainable parameters and hyperparameters, including geometry priors and loss weights. It is worth mentioning that this loss has already been used in outdoor 3D object detection [34]. Recently, [6] reported results of VoteNet trained with axis-aligned IoU loss on ScanNet.

Tab. 2 shows that replacing the standard parametrization with Mobius one boosts VoteNet and ImVoteNet mAP@0.5 by approximately 4%.

ImVoxelNet does not use a classification+regression scheme to estimate heading angle but predicts its value directly in a single step. Since the original ImVoxelNet uses the rotated IoU loss, we do not need to remove redundant losses, only to change the parametrization. Again, the Mobius parametrization helps to obtain the best results, even though the superiority is minor.

GSDN anchors. Next, we study GSDN anchors to prove that the generalization ability of anchor-based models is limited. According to Tab. 3, mAP@0.5 drops dramatically by 12% if GSDN is trained in an anchor-free setting (which is equivalent to using one anchor). In other words, without domain-specific guidance in the form of anchors, GSDN demonstrates a poor performance; hence, we claim this method to be inflexible and non-generalized. For a fair comparison, we evaluate FCAF3D with the same backbone, and it outperforms GSDN by a huge margin, achieving twice as large mAP value.

5.3. Ablation Study

In this section, we discuss the design choices in FCAF3D and investigate how they affect final metrics when applied independently in ablation studies. We run experiments with varying voxel size, the number of points in a point cloud $N_{\rm pts}$, the number of locations selected by center sampling, and with and without centerness. The results of ablation studies are aggregated in Tab. 4 for all the benchmarks.

Voxel size. Expectedly, with an increasing voxel size, accuracy goes down. We try voxels of 0.03, 0.02, and 0.01 m. We do not experiment with smaller values since inference would take too much time. We attribute the notable

Method	Input	mAP@0.25	mAP@0.5
VoteNet [22]		57.7	-
Reimpl. [6]		59.1	35.8
Reimpl. w/ IoU loss	PC		
w/ naive param.	PC	61.1 (60.3)	38.4 (37.7)
w/ sin-cos param.		60.7 (59.8)	37.1 (36.4)
w/ Mobius param.		61.1 (60.5)	40.4 (39.5)
ImVoteNet [21]		63.4	-
Reimpl. [6]		64.0	37.8
Reimpl. w/ IoU loss	RGB		
w/ naive param.	+PC	64.2 (63.9)	39.1 (38.3)
w/ sin-cos param.		64.6 (64.0)	39.9 (37.8)
w/ Mobius param.		64.6 (64.1)	40.8 (39.8)
ImVoxelNet [24]		40.7	-
w/ naive param.	RGB	41.3 (40.4)	13.8 (13.0)
w/ sin-cos param.	KUB	41.3 (40.5)	13.2 (12.8)
w/ Mobius param.		41.5 (40.6)	14.6 (14.0)
FCAF3D			
w/ naive param.	PC	63.8 (63.5)	46.8 (46.2)
w/ sin-cos param.	I C	63.9 (63.6)	48.2 (47.3)
w/ Mobius param.		64.2 (63.8)	48.9 (48.2)

Table 2. Results of several existing 3D object detection methods that accept inputs of different modalities, with different OBB parametrization on the SUN RGB-D dataset. For FCAF3D, the reported metric value is the best across 25 trials; the average value is given in brackets. For other methods, we report results from the original papers and also the results obtained through our experiments with MMdetection3D-based re-implementations (marked as Reimpl). PC stands for a point cloud.

Paalshana	Voxel	Scenes	mAP	
Backbone	size	per sec.	0.25 0.5	5
	0.05	20.1	62.8 34.	.8
IIDD agNat24	0.05	20.4	56.3 22.	.7
nDResnet34	0.05	21.8	46.0 28.	.6
	0.01	8.0	70.7 56.	0.
HDResNet34:3	0.01	12.2	69.8 53.	.6
HDResNet34:2	0.02	31.5	63.1 46.	.8
		Backbone size	HDResNet34: Size per sec. 0.05 20.1 0.05 20.4 0.05 21.8 0.01 8.0 HDResNet34:3 0.01 12.2	Backbone size per sec. 0.25 0. HDResNet34 0.05 20.1 62.8 34 0.05 20.4 56.3 22 0.05 21.8 46.0 28 0.01 8.0 70.7 56 HDResNet34:3 0.01 12.2 69.8 53

Table 3. Results of fully convolutional 3D object detection methods that accept point clouds on ScanNet.

gap in mAP between voxel sizes of 0.01 and 0.02 m to the presence of *almost flat* objects, such as doors, pictures, and whiteboards. Namely, with a voxel size of 2 cm, the head would output locations with 16 cm tolerance, but the *almost flat* objects could be less than 16 cm by one of the dimensions. Accordingly, we observe a decrease in accuracy for larger voxel sizes.

Number of points. Similar to 2D images, subsampled point clouds are sometimes referred to as *low-resolution* ones. Accordingly, they contain less information than their

Ablating	Value	Scan	Net	SUN R	GB-D	S3I	DIS
parameter	value	mAP@0.25	mAP@0.5	mAP@0.25	mAP@0.5	mAP@0.25	mAP@0.5
Voxel	0.01	71.5 (70.7)	57.3 (56.0)	64.2 (63.8)	48.9 (48.2)	66.7 (64.9)	45.9 (43.8)
size	0.02	66.3 (65.8)	49.4 (48.6)	62.3 (62.0)	46.3 (45.5)	61.0 (58.5)	43.8 (38.5)
Size	0.03	59.6 (59.2)	42.6 (41.6)	60.4 (59.7)	41.6 (41.0)	55.4 (53.3)	38.6 (35.0)
Number of	20k	69.0 (68.1)	52.8 (52.0)	63.0 (62.5)	46.9 (46.5)	60.1 (58.8)	45.1 (40.1)
	40k	67.6 (66.7)	53.6 (52.2)	63.4 (63.1)	47.2 (46.6)	63.7 (61.2)	44.8 (42.2)
points	100k	71.5 (70.7)	57.3 (56.0)	64.2 (63.8)	48.9 (48.2)	66.7 (64.9)	45.9 (43.8)
Centerness	No	71.0 (70.4)	56.1 (55.1)	63.8 (63.3)	48.2 (47.5)	67.9 (65.5)	46.0 (43.5)
Centerness	Yes	71.5 (70.7)	57.3 (56.0)	64.2 (63.8)	48.9 (48.2)	66.7 (64.9)	45.9 (43.8)
Center	9	70.6 (70.1)	55.7 (55.0)	63.8 (63.3)	48.6 (48.2)	66.5 (63.6)	44.4 (42.5)
	18	71.5 (70.7)	57.3 (56.0)	64.2 (63.8)	48.9 (48.2)	66.7 (64.9)	45.9 (43.8)
sampling	27	70.2 (69.7)	55.7 (54.1)	64.3 (63.8)	48.7 (47.9)	65.1 (63.2)	43.6 (41.7)

Table 4. Results of ablation studies on the voxel size, the number of points (which equals the number of voxels N_{vox} in pruning), centerness, and center sampling in FCAF3D. The better options are marked bold; actually, these are the default options used to obtain the results in Tab. 1 above. The reported metric value is the best across 25 trials; the average value is given in brackets.

high-resolution versions. As can be expected, the fewer the points, the lower is detection accuracy. In this series of experiments, we sample 20k, 40k, and 100k points from the entire point cloud, and the obtained metric values revealed a clear dependency between the number of points and mAP. We do not consider larger $N_{\rm pts}$ values to be on a par with the existing methods (specifically, GSDN [10] uses all points in a point cloud, GroupFree [17] samples 50k points, VoteNet [22] selects 40k points for ScanNet and 20k for SUN RGB-D). We use $N_{\rm vox} = N_{\rm pts}$ to guide pruning in the neck. When $N_{\rm vox}$ exceeds 100k, the inference time increases due to growing sparsity in the neck, while the accuracy improvement is negligible. So we restrict our grid search for $N_{\rm pts}$ with 100k and use it as a default value regarding the obtained results.

Centerness. Using centerness improves mAP for the ScanNet and SUN RGB-D datasets. For S3DIS, the results are controversial: the better mAP@0.5 is balanced with a minor decrease of mAP@0.25. Nevertheless, we analyze the results altogether, so we can consider centerness a helpful feature with a small positive effect on the mAP, almost reaching 1% of mAP@0.5 on ScanNet.

Center sampling. Finally, we study the number of locations selected in center sampling. We select 9 locations, as proposed in FCOS [26], the entire set of 27 locations, as in ImVoxelNet [24], and 18 being an average of these options. The latter appeared to be the best choice that allows achieving higher mAP on all the benchmarks.

5.4. Inference Speed

Compared to standard convolutions, sparse convolutions are time- and memory-efficient. GSDN authors claim that with sparse convolutions, they process a scene with 78M points covering about 14,000 m³ within a single fully convolutional feed-forward pass, using only 5G of GPU mem-

ory. FCAF3D uses the same sparse convolutions and the same backbone as GSDN. However, as can be seen in Tab. 3, the default FCAF3D is slower than GSDN. This is due to the smaller voxel size: we use 0.01m for a proper multilevel assignment while GSDN uses 0.05m.

To build the fastest method, we conduct experiments with HDResNet34:3 and HDResNet34:2 with only three and two feature levels, respectively. With these modifications, FCAF3D is faster on inference than GSDN. The comparison is shown graphically in Fig. 1.

For a fair comparison, we re-measure inference speed for GSDN and voting-based methods, as point grouping operation and sparse convolutions have become much faster since the initial release of these methods. In performance tests, we opt for implementations based on the MMdetection3D [6] framework to mitigate codebase differences. The reported inference speed for all methods is measured on the same single GPU so they can be directly compared.

6. Conclusion

We have introduced FCAF3D, a first-in-class fully convolutional anchor-free 3D object detection method for indoor scenes. The proposed method significantly outperforms the previous state-of-the-art on the challenging indoor SUN RGB-D, ScanNet, and S3DIS benchmarks in terms of both mAP and inference speed. We have also proposed a novel oriented bounding box parametrization and shown that it improves detection accuracy for several existing 3D object detection methods. Moreover, the proposed parametrization allows avoiding any prior assumptions about objects, thus reducing the number of hyperparameters.

Acknowledgment. We would like to thank Alexey Rukhovich for useful discussions on topology.

References

- [1] Iro Armeni, Ozan Sener, Amir R Zamir, Helen Jiang, Ioannis Brilakis, Martin Fischer, and Silvio Savarese. 3d semantic parsing of large-scale indoor spaces. In *Proceedings of the IEEE Conference on Computer Vision and Pattern Recognition*, pages 1534–1543, 2016. 2, 5
- [2] Jintai Chen, Biwen Lei, Qingyu Song, Haochao Ying, Danny Z Chen, and Jian Wu. A hierarchical graph network for 3d object detection on point clouds. In *Proceedings of* the IEEE/CVF conference on computer vision and pattern recognition, pages 392–401, 2020. 6
- [3] Kai Chen, Jiaqi Wang, Jiangmiao Pang, Yuhang Cao, Yu Xiong, Xiaoxiao Li, Shuyang Sun, Wansen Feng, Ziwei Liu, Jiarui Xu, et al. Mmdetection: Open mmlab detection toolbox and benchmark. arXiv preprint arXiv:1906.07155, 2019.
- [4] Bowen Cheng, Lu Sheng, Shaoshuai Shi, Ming Yang, and Dong Xu. Back-tracing representative points for votingbased 3d object detection in point clouds. In *Proceedings of* the IEEE/CVF Conference on Computer Vision and Pattern Recognition, pages 8963–8972, 2021. 2, 6
- [5] Christopher Choy, Jun Young Gwak, and Silvio Savarese. 4d spatio-temporal convnets: Minkowski convolutional neural networks. In *Proceedings of the IEEE Conference on Com*puter Vision and Pattern Recognition, pages 3075–3084, 2019. 3
- [6] MMDetection3D Contributors. MMDetection3D: Open-MMLab next-generation platform for general 3D object detection. https://github.com/open-mmlab/mmdetection3d, 2020. 5, 7, 8
- [7] Angela Dai, Angel X Chang, Manolis Savva, Maciej Halber, Thomas Funkhouser, and Matthias Nießner. Scannet: Richly-annotated 3d reconstructions of indoor scenes. In *Proceedings of the IEEE conference on computer vision and pattern recognition*, pages 5828–5839, 2017. 2, 5
- [8] Francis Engelmann, Martin Bokeloh, Alireza Fathi, Bastian Leibe, and Matthias Nießner. 3d-mpa: Multi-proposal aggregation for 3d semantic instance segmentation. In Proceedings of the IEEE/CVF conference on computer vision and pattern recognition, pages 9031–9040, 2020. 6
- [9] Zheng Ge, Songtao Liu, Zeming Li, Osamu Yoshie, and Jian Sun. Ota: Optimal transport assignment for object detection. In *Proceedings of the IEEE/CVF Conference on Computer Vision and Pattern Recognition*, pages 303–312, 2021. 4
- [10] JunYoung Gwak, Christopher Choy, and Silvio Savarese. Generative sparse detection networks for 3d single-shot object detection. In *Computer Vision–ECCV 2020: 16th European Conference, Glasgow, UK, August 23–28, 2020, Proceedings, Part IV 16*, pages 297–313. Springer, 2020. 1, 2, 5, 6, 7, 8, 11, 12
- [11] Kaiming He, Xiangyu Zhang, Shaoqing Ren, and Jian Sun. Deep residual learning for image recognition. In *Proceedings of the IEEE conference on computer vision and pattern recognition*, pages 770–778, 2016. 3
- [12] Ji Hou, Angela Dai, and Matthias Nießner. 3d-sis: 3d semantic instance segmentation of rgb-d scans. In *Proceedings of*

- the IEEE/CVF Conference on Computer Vision and Pattern Recognition, pages 4421–4430, 2019. 2
- [13] Alex H Lang, Sourabh Vora, Holger Caesar, Lubing Zhou, Jiong Yang, and Oscar Beijbom. Pointpillars: Fast encoders for object detection from point clouds. In *Proceedings of* the IEEE/CVF Conference on Computer Vision and Pattern Recognition, pages 12697–12705, 2019. 2, 4
- [14] Bo Li. 3d fully convolutional network for vehicle detection in point cloud. In 2017 IEEE/RSJ International Conference on Intelligent Robots and Systems (IROS), pages 1513–1518. IEEE, 2017. 2
- [15] Tsung-Yi Lin, Priya Goyal, Ross Girshick, Kaiming He, and Piotr Dollár. Focal loss for dense object detection. In *Proceedings of the IEEE international conference on computer vision*, pages 2980–2988, 2017. 3
- [16] Zechen Liu, Zizhang Wu, and Roland Tóth. Smoke: Single-stage monocular 3d object detection via keypoint estimation. In Proceedings of the IEEE/CVF Conference on Computer Vision and Pattern Recognition Workshops, pages 996–997, 2020. 4, 7
- [17] Ze Liu, Zheng Zhang, Yue Cao, Han Hu, and Xin Tong. Group-free 3d object detection via transformers. In *Proceedings of the IEEE/CVF International Conference on Computer Vision (ICCV)*, pages 2949–2958, 2021. 2, 5, 6, 8, 11, 12
- [18] Daniel Maturana and Sebastian Scherer. Voxnet: A 3d convolutional neural network for real-time object recognition. In 2015 IEEE/RSJ International Conference on Intelligent Robots and Systems (IROS), pages 922–928. IEEE, 2015. 2
- [19] Ishan Misra, Rohit Girdhar, and Armand Joulin. An end-to-end transformer model for 3d object detection. In *Proceedings of the IEEE/CVF International Conference on Computer Vision*, pages 2906–2917, 2021. 1, 2, 4, 6
- [20] James R Munkres. Topology, 2000. 5
- [21] Charles R Qi, Xinlei Chen, Or Litany, and Leonidas J Guibas. Imvotenet: Boosting 3d object detection in point clouds with image votes. In *Proceedings of the IEEE/CVF conference on computer vision and pattern recognition*, pages 4404–4413, 2020. 4, 7
- [22] Charles R Qi, Or Litany, Kaiming He, and Leonidas J Guibas. Deep hough voting for 3d object detection in point clouds. In *Proceedings of the IEEE/CVF International Conference on Computer Vision*, pages 9277–9286, 2019. 1, 2, 4, 5, 6, 7, 8, 11, 12
- [23] Charles R Qi, Hao Su, Kaichun Mo, and Leonidas J Guibas. Pointnet: Deep learning on point sets for 3d classification and segmentation. In *Proceedings of the IEEE conference* on computer vision and pattern recognition, pages 652–660, 2017. 2
- [24] Danila Rukhovich, Anna Vorontsova, and Anton Konushin. Imvoxelnet: Image to voxels projection for monocular and multi-view general-purpose 3d object detection. arXiv preprint arXiv:2106.01178, 2021. 3, 4, 7, 8
- [25] Shuran Song, Samuel P Lichtenberg, and Jianxiong Xiao. Sun rgb-d: A rgb-d scene understanding benchmark suite. In *Proceedings of the IEEE conference on computer vision and pattern recognition*, pages 567–576, 2015. 2, 5

- [26] Zhi Tian, Chunhua Shen, Hao Chen, and Tong He. Fcos: Fully convolutional one-stage object detection. In *Proceedings of the IEEE/CVF international conference on computer vision*, pages 9627–9636, 2019. 1, 3, 4, 5, 8
- [27] Tai Wang, Xinge Zhu, Jiangmiao Pang, and Dahua Lin. Fcos3d: Fully convolutional one-stage monocular 3d object detection. *arXiv preprint arXiv:2104.10956*, 2021. 3
- [28] Qian Xie, Yu-Kun Lai, Jing Wu, Zhoutao Wang, Dening Lu, Mingqiang Wei, and Jun Wang. Venet: Voting enhancement network for 3d object detection. In *Proceedings of the IEEE/CVF International Conference on Computer Vi*sion, pages 3712–3721, 2021. 2, 6
- [29] Qian Xie, Yu-Kun Lai, Jing Wu, Zhoutao Wang, Yiming Zhang, Kai Xu, and Jun Wang. Mlcvnet: Multi-level context votenet for 3d object detection. In *Proceedings of the IEEE/CVF conference on computer vision and pattern recognition*, pages 10447–10456, 2020. 2, 6
- [30] Yan Yan, Yuxing Mao, and Bo Li. Second: Sparsely embedded convolutional detection. Sensors, 18(10):3337, 2018. 2,
- [31] Tianwei Yin, Xingyi Zhou, and Philipp Krahenbuhl. Center-based 3d object detection and tracking. In Proceedings of the IEEE/CVF Conference on Computer Vision and Pattern Recognition, pages 11784–11793, 2021. 2
- [32] Shifeng Zhang, Cheng Chi, Yongqiang Yao, Zhen Lei, and Stan Z Li. Bridging the gap between anchor-based and anchor-free detection via adaptive training sample selection. In *Proceedings of the IEEE/CVF conference on computer vision and pattern recognition*, pages 9759–9768, 2020. 1, 4, 5
- [33] Zaiwei Zhang, Bo Sun, Haitao Yang, and Qixing Huang. H3dnet: 3d object detection using hybrid geometric primitives. In *European Conference on Computer Vision*, pages 311–329. Springer, 2020. 2, 4, 6, 11, 12
- [34] Dingfu Zhou, Jin Fang, Xibin Song, Chenye Guan, Junbo Yin, Yuchao Dai, and Ruigang Yang. Iou loss for 2d/3d object detection. In 2019 International Conference on 3D Vision (3DV), pages 85–94. IEEE, 2019. 7
- [35] Yin Zhou and Oncel Tuzel. Voxelnet: End-to-end learning for point cloud based 3d object detection. In *Proceedings of the IEEE conference on computer vision and pattern recognition*, pages 4490–4499, 2018. 2

A. Additional Comments on Mobius Parametrization

Comments on Eq. 3. The OBB heading angle θ is typically defined as an angle between x-axis and a vector towards a center of one of OBB faces. If a frontal face exists, then θ is defined unambiguously; however, this is not the case for some indoor objects. If a frontal face cannot be chosen unequivocally, there are four possible representations for a single OBB. The heading angle describes a rotation within the xy plane around z-axis w.r.t. the OBB center. Therefore, the OBB center (x, y, z), height h, and the OBB size s = w + l are the same for all representations. Meanwhile, the ratio $q = \frac{w}{l}$ of the frontal and lateral OBB faces and the heading angle θ do vary. Specifically, there are four options for the heading angle: θ , $\theta + \frac{\pi}{2}$, $\theta + \pi$, $\theta + \frac{3\pi}{2}$. Swapping frontal and lateral faces gives two ratio options: q and $\frac{1}{q}$. Overall, there are four different tuples (q, θ) for the same OBB:

$$(q,\theta), (\frac{1}{q}, \theta + \frac{\pi}{2}), (q,\theta + \pi), (\frac{1}{q}, \theta + \frac{3\pi}{2}).$$

Verification of Eq. 4. Here, we prove that four different representations of the same OBB from Eq. 3 map to the same point on a Mobius strip by Eq. 4.

$$\begin{aligned} (q,\,\theta) &\mapsto (\ln(q)\sin(2\theta),\,\ln(q)\cos(2\theta),\,\sin(4\theta),\,\cos(4\theta)) \\ (\frac{1}{q},\,\theta+\frac{\pi}{2}) &\mapsto (\ln(\frac{1}{q})\sin(2\theta+\pi),\,\ln(\frac{1}{q})\cos(2\theta+\pi),\,\sin(4\theta+2\pi),\,\cos(4\theta+2\pi)) \\ &= (\ln(q)\sin(2\theta),\,\ln(q)\cos(2\theta),\,\sin(4\theta),\,\cos(4\theta)) \\ (q,\,\theta+\pi) &\mapsto (\ln(q)\sin(2\theta+2\pi)),\,\ln(q)\cos(2\theta+2\pi),\,\sin(4\theta+4\pi),\,\cos(4\theta+4\pi)) \\ &= (\ln(q)\sin(2\theta),\,\ln(q)\cos(2\theta),\,\sin(4\theta),\,\cos(4\theta)) \\ (\frac{1}{q},\,\theta+\frac{3\pi}{2}) &\mapsto (\ln(\frac{1}{q})\sin(2\theta+3\pi)),\,\ln(\frac{1}{q})\cos(2\theta+3\pi),\,\sin(4\theta+6\pi),\,\cos(4\theta+6\pi) \\ &= (\ln(q)\sin(2\theta),\,\ln(q)\cos(2\theta),\,\sin(4\theta),\,\cos(4\theta)) \end{aligned}$$

B. Per-category results

ScanNet. Tab. 5 contains per-category AP@0.25 scores for 18 object categories for the ScanNet dataset. For 12 out of 18 categories, FCAF3D outperforms other methods. The largest quality gap can be observed for *window* (60.2 against 53.7), *picture* (29.9 against 18.6), and *other furniture* (65.4 against 56.4) categories.

Method	cab	bed	chair	sofa	tabl	door	wind	bkshf	pic	cntr	desk	curt	fridg	showr	toil	sink	bath	ofurn	mAP
VoteNet [22]	36.3	87.9	88.7	89.6	58.8	47.3	38.1	44.6	7.8	56.1	71.7	47.2	45.4	57.1	94.9	54.7	92.1	37.2	58.7
GSDN [10]	41.6	82.5	92.1	87.0	61.1	42.4	40.7	51.5	10.2	64.2	71.1	54.9	40.0	70.5	100	75.5	93.2	53.1	62.8
H3DNet [33]	49.4	88.6	91.8	90.2	64.9	61.0	51.9	54.9	18.6	62.0	75.9	57.3	57.2	75.3	97.9	67.4	92.5	53.6	67.2
GroupFree [17]	52.1	92.9	93.6	88.0	70.7	60.7	53.7	62.4	16.1	58.5	80.9	67.9	47.0	76.3	99.6	72.0	95.3	56.4	69.1
FCAF3D	57.2	87.0	95.0	92.3	70.3	61.1	60.2	64.5	29.9	64.3	71.5	60.1	52.4	83.9	99.9	84.7	86.6	65.4	71.5

Table 5. Per-category AP@0.25 scores for 18 object categories from the ScanNet dataset.

Tab. 6 shows per-category AP@0.5 scores. According to the reported values, FCAF3D is the best at detecting objects of 13 out of 18 categories. The most significant improvement is achieved for *cabinet* (35.8 against 26.0), *sofa* (85.2 against 70.7), *picture* (17.9 against 7.8), shower (64.2 against 44.1), and *sink* (52.6 against 37.4).

Method	cab	bed	chair	sofa	tabl	door	wind	bkshf	pic	cntr	desk	curt	fridg	showr	toil	sink	bath	ofurn	mAP
VoteNet [22]	8.1	76.1	67.2	68.8	42.4	15.3	6.4	28.0	1.3	9.5	37.5	11.6	27.8	10.0	86.5	16.8	78.9	11.7	33.5
GSDN [10]	13.2	74.9	75.8	60.3	39.5	8.5	11.6	27.6	1.5	3.2	37.5	14.1	25.9	1.4	87.0	37.5	76.9	30.5	34.8
H3DNet [33]	20.5	79.7	80.1	79.6	56.2	29.0	21.3	45.5	4.2	33.5	50.6	37.3	41.4	37.0	89.1	35.1	90.2	35.4	48.1
GroupFree [17]	26.0	81.3	82.9	70.7	62.2	41.7	26.5	55.8	7.8	34.7	67.2	43.9	44.3	44.1	92.8	37.4	89.7	40.6	52.8
FCAF3D	35.8	81.5	89.8	85.0	62.0	44.1	30.7	58.4	17.9	31.3	53.4	44.2	46.8	64.2	91.6	52.6	84.5	57.1	57.3

Table 6. AP@0.50 scores for 18 object categories from the ScanNet dataset.

SUN RGB-D. Per-category AP@0.25 scores for the 10 most common object categories for the SUN RGB-D benchmark are reported in Tab. 7. Compared to other methods, FCAF3D is more accurate at detecting objects of 7 out of 10 categories. In

this experiment, the quality gap is not so dramatic: it equals 4.1 % for *desk* and 5.2 % for *night stand*; for the rest categories, it does not exceed 2 %. FCAF3D achieves a 1.2 % better mAP@0.25 compared to the closest competitor GroupFree.

Method	bath	bed	bkshf	chair	desk	dresser	nstand	sofa	table	toilet	mAP
VoteNet [22]	74.4	83.0	28.8	75.3	22.0	29.8	62.2	64.0	47.3	90.1	57.7
H3DNet [33]	73.8	85.6	31.0	76.7	29.6	33.4	65.5	66.5	50.8	88.2	60.1
GroupFree [17]	80.0	87.8	32.5	79.4	32.6	36.0	66.7	70.0	53.8	91.1	63.0
FCAF3D	79.0	88.3	33.0	81.1	34.0	40.1	71.9	69.7	53.0	91.3	64.2

Table 7. AP@0.25 scores for 10 object categories from the SUN RGB-D dataset.

For SUN RGB-D, the superiority of the proposed method is more noticeable when analyzing on per-category AP@0.5. As shown in Tab. 8, FCAF3D outperforms the competitors for 9 out of 10 object categories. For some categories, there is a significant margin: e.g., 30.1 against 21.9 for *dresser*, 59.8 against 49.8 for *night stand*, and 35.5 against 29.2 for *table*. Respectively, FCAF3D surpasses other methods by more than 3.5 % in terms of mAP@0.5.

Method	bath	bed	bkshf	chair	desk	dresser	nstand	sofa	table	toilet	mAP
H3DNet [33]	47.6	52.9	8.6	60.1	8.4	20.6	45.6	50.4	27.1	69.1	39.0
GroupFree [17]	64.0	67.1	12.4	62.6	14.5	21.9	49.8	58.2	29.2	72.2	45.2
FCAF3D	66.2	69.8	11.6	68.8	14.8	30.1	59.8	58.2	35.5	74.5	48.9

Table 8. AP@0.50 scores for 10 object categories from the SUN RGB-D dataset.

S3DIS. The results of the proposed method in comparison with GSDN are presented in Tab. 9 and Tab. 10. In terms of AP@0.25, FCAF3D is far more accurate when detecting *sofas*, *bookcases*, and *whiteboards*. Most notably, FCAF3D achieves an impressive AP@0.25 of 92.4 for the *sofa* category, leaving GSDN with AP@0.25 of 20.8 far behind. The difference in mAP in favor of the proposed method is almost 19 %.

Method						
GSDN [10]						
FCAF3D	69.7	97.4	92.4	36.7	37.3	66.7

Table 9. Per-category AP@0.25 scores for 5 object categories from the S3DIS dataset.

In terms of AP@0.5, FCAF3D outperforms GSDN by a large margin for each category. Similar to AP@0.25, the accuracy gap for the *sofa* category is the most dramatic: with an AP@0.25 of 70.1, FCAF3D is an order of magnitude more accurate than GSDN, which has only 6.1. Accordingly, FCAF3D has an approximately 1.8 times larger mAP compared to GSDN.

				bkcase	board	mAP
GSDN [10]	36.6	75.3	6.1	6.5	1.2	
FCAF3D	45.4	88.3	70.1	19.5	5.6	45.9

Table 10. AP@0.50 scores for 5 object categories from the S3DIS dataset.

C. Visualization

This section contains additional visualizations of the results of 3D object detection for all three benchmarks. The ground truth and estimated 3D object bounding boxes are drawn over the corresponding point clouds. Objects of different categories are marked with different colors.

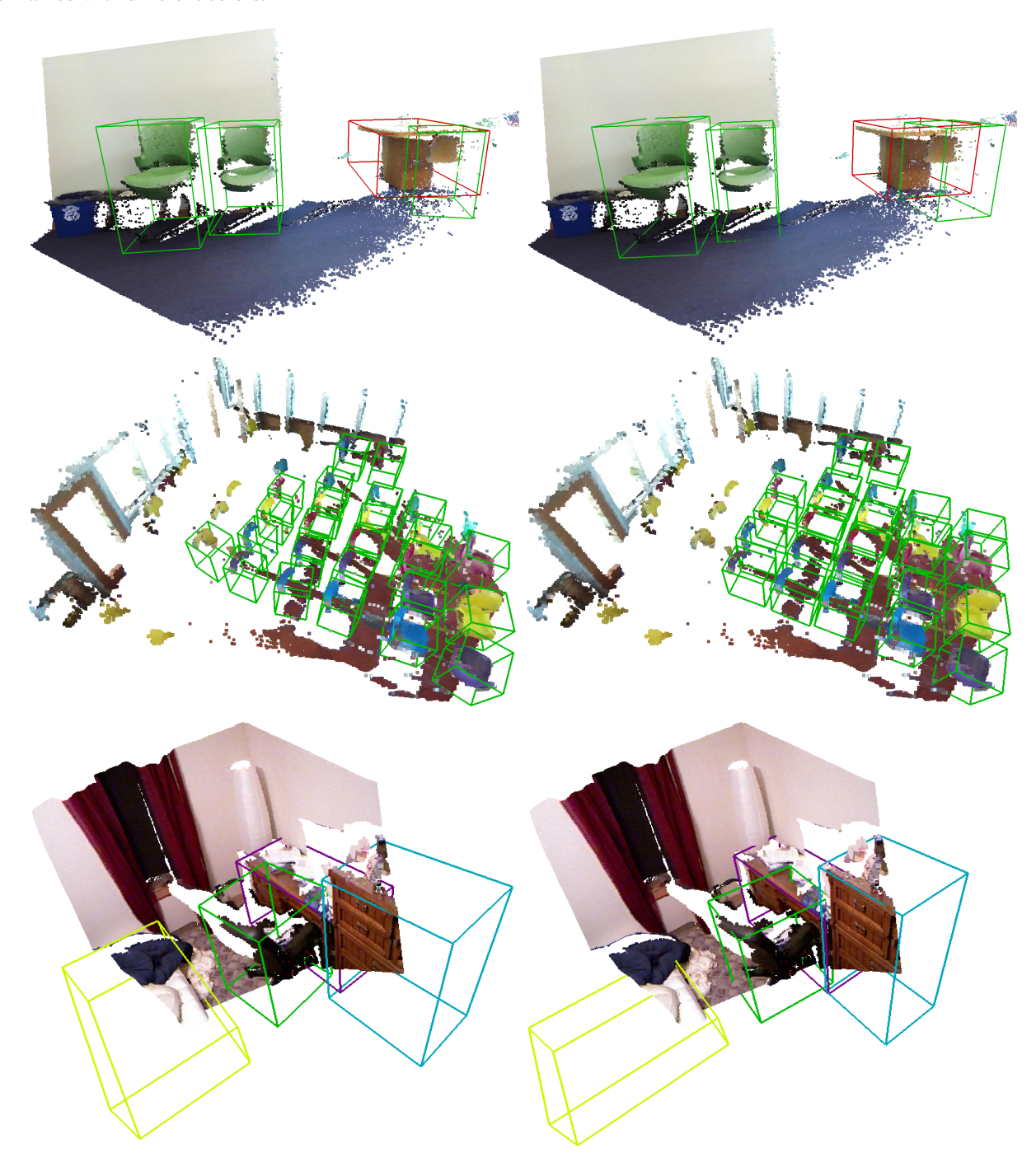


Figure 7. The point cloud from SUN RGB-D with OBBs. The color of a bounding box denotes the object category: bed, chair, desk, dresser, table (only categories that are present in the pictures are listed). Left: estimated with FCAF3D, right: ground truth.

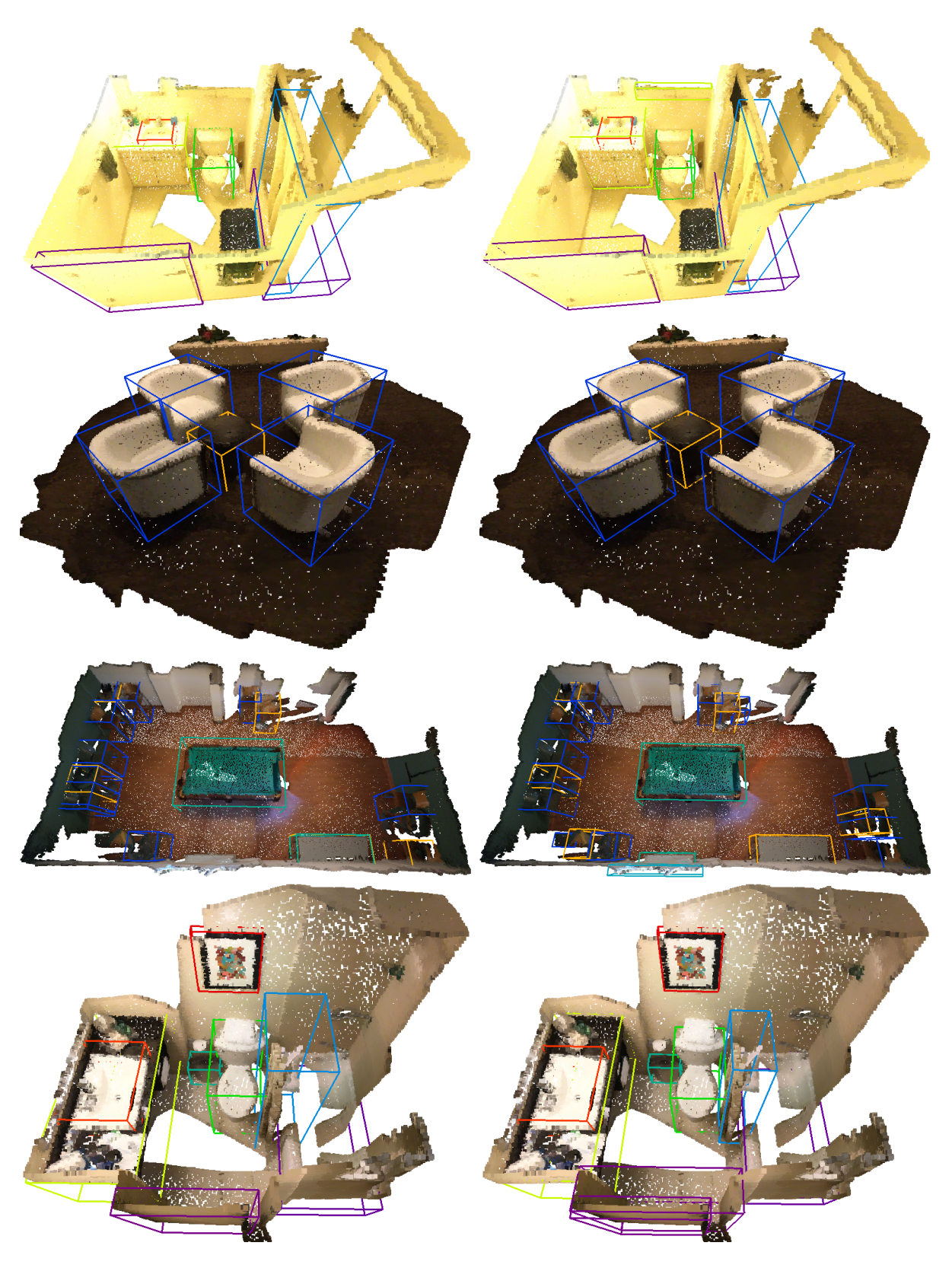


Figure 8. The point cloud from ScanNet with AABBs. The color of a bounding box denotes the object category: cabinet, chair, sofa, table, door, window, bookshelf, picture, counter, desk, shower curtain, toilet, sink, bathtub, other furniture (only categories that are present in the pictures are listed). Left: estimated with FCAF3D, right: ground truth.



Figure 9. The point cloud from S3DIS with AABBs. The color of a bounding box denotes the object category: table, chair, sofa, bookcase, whiteboard. Left: estimated with FCAF3D, right: ground truth.